Environmental Health Perspectives
Vol. 63, pp. 11-24, 1985

Ambient Sulfate Aerosol Deposition in Man: Modeling the Influence of Hygroscopicity

by T. Blayne Martonen,* Andrew E. Barnett,† and Frederick J. Miller*

Atmospheric sulfate aerosols [H_2SO_4, $(NH_4)_2SO_4$, and NH_4HSO_4] are of international concern because of their global prevalence and potential irritant or toxic effects on humans. To assess hazards following inhalation exposure, the total dose delivered to the human respiratory tract and its regional distribution must be determined. The mass median aerodynamic diameter of the inhaled aerosol will influence the sites of deposition in the respiratory tract. Atmospheric sulfate aerosols are hygroscopic and will have changing particle sizes and densities as they absorb water vapor in the humid environment of the human respiratory tract. Experimental and theoretical data that describe particle size as a function of temperature and relative humidity were used in computer subroutines of an aerosol deposition model in order to calculate the dose dispersion of H_2SO_4, $(NH_4)_2SO_4$, and NH_4HSO_4 aerosols in man. Different temperature and relative humidity environments that approximately correspond to nasal and oral breathing were studied. The predicted deposition patterns are very different from those of nonhygroscopic aerosols with identical inhaled mass median aerodynamic diameter values.

Introduction

The origin, properties, and distribution of sulfate aerosols in the ambient atmosphere have been (*1*), and continue to be, studied. Present atmospheric sulfate levels and their potential toxic or irritant effects following inhalation exposure are foci in human health studies related to urban air pollution (*2*).

It is important to know the deposition sites of inhaled particulate matter within the respiratory tract when assessing the health effects of atmospheric contaminants. Inhalation exposure experiments with human test subjects have established that nonhygroscopic particle deposition probabilities can be expressed as a function of the following two properties of an inspired aerosol: the mass median aerodynamic diameter (MMAD) and geometric standard deviation (σ_g) (*3,4*).

A hygroscopic particle may change in size, shape, and density due to water vapor uptake in humid respiratory passages. Consequently, a hygroscopic aerosol's MMAD may vary with location in the respiratory tract, and the dose delivered may be different from that of a nonhygroscopic aerosol of like size distribution.

In this report, we discuss a theoretical model of aerosol behavior in the human respiratory tract. The model permits relative analyses of salient factors that influence particulate deposition. Equations proposed by Martonen (*5*) that describe the deposition efficiencies of inertial impaction, sedimentation, and diffusion mechanisms are used.

Three tracheobronchial (TB) tree morphologies (*6–8*) were evaluated as representations of the human lung. The experimental data that quantitate nonhygroscopic particle deposition efficiencies in human test subjects summarized by Lippmann et al. (*9*) were compared to calculated values for the three morphologies. Findings suggest that the symmetric, dichotomously branching, modified-Weibel geometry proposed by Soong et al. (*8*) suitably describes aerosol behavior in human airways.

The equilibrium sizes and densities of H_2SO_4, $(NH_4)_2SO_4$, and NH_4HSO_4 particles measured over a range of relative humidity values by Tang (*10*), Tang and Munkelwitz (*11*), and Tang et al. (*12*) were incorporated into our analytical model to study the influence of hygroscopicity on the fate of airborne contaminants of health-effects concern. It was determined that the hygroscopic character of ambient sulfate aerosols may significantly affect total dose delivered to the respiratory tract as well as dose distribution among airways.

Aerosol Deposition Model

Mathematical computation of aerosol deposition requires definition of the following:

- Respiratory tract geometry
- TB airflow dynamics (including the influence of the laryngeal jet)

*Toxicology Branch, Health Effects Research Laboratory, U.S. Environmental Protection Agency, Research Triangle Park, NC 27711.

†Northrop Services, Inc., Environmental Sciences, P. O. Box 12313, Research Triangle Park, NC 27709.

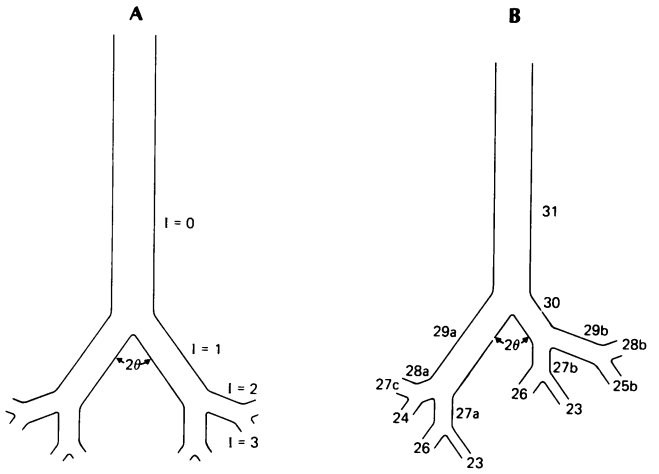

FIGURE 1. A comparision of (*A*) symmetric Weibel (*6*) and (*B*) asymmetric Horsfield et al. (*7*) large airway geometries. Bifurcation angle is denoted by 2θ.

- Formulae that describe particle deposition efficiencies
- Temperature (T) and relative humidity (RH) profiles
- For hygroscopic materials, data that describe size and density variation with T and RH environment

TB Morphologies

Weibel (*6*) has proposed a simple morphology for the human TB tree. It is a symmetric, dichotomous, branching system of 17 generations of conducting airways numbered in descending order from the trachea, which is generation $I = 0$. The terminal unalveolated bronchiole is $I = 16$. Beginning with the trachea, each "parent" airway branches into two identical "daughter" airways; there are 2^I airways in each generation. The Soong et al. (*8*) morphology is a statistical description intended to account for structural and dimensional variations within the human TB tree among a population. The branching scheme is the same as Weibel's (*6*), but airway dimensions differ.

Horsfield et al. (*7*) proposed a complex asymmetric human lung morphology. Airways of different dimensions exist in the same TB tree generation. Moreover, the branching scheme is a dichotomous spatial network that is defined in terms of airway "orders." [Note: "order" is related, but not uniquely, to airway dimensions (*7*).] Four different bifurcating patterns were used to simulate various regions of the human TB tree. For these reasons, it has been proposed as a more physiologically realistic model of the human lung.

The Weibel (*6*) and Horsfield et al. (*7*) morphologies are contrasted in Figure 1; for simplicity, only upper airways are shown. Distinctions between the symmetric and asymmetric geometries are obvious upon comparison of Figures 1*A* and 1*B*. In Figure 1*B*, airways are labeled by their designated "order" identification numbers for the readers' reference.

Airway Flow Dynamics

The dynamics of airflow within idealized airway models, replica casts, and the human lung has been extensively reviewed (*13*). In this report we will comment on some of the studies most applicable to our work.

In Table 1, morphological data of Soong et al. (*8*) are related to commonly used parameters for the classification of fluid dynamics in idealized tubes (long, straight, rigid, smooth-walled tubes of circular cross-section). Airway generations $I = 0$, 1, 2, 3, and 4 correspond to the trachea and to the main, lobar, segmental, and first subsegmental bronchi, respectively, of the human lung. The 15-, 30-, and 60-L/min tracheal flow rates, $Q(0)$, correspond to tidal volumes of 500, 1000, and 2000 cm^3, respectively. The length L necessary to attain a parabolic air velocity profile from laminar plug flow in an idealized tube of diameter D is defined (*14*) by the relation:

$$1 \geq 0.06D\mathrm{Re}/L$$

The Reynolds number, Re, is defined as $\mathrm{Re} = DU\eta^{-1}$, where U and η are the mean velocity and kinematic viscosity of air, respectively. Laminar-to-turbulent transition is generally thought to occur at an Re of approximately 2200. The equation may be put into the form

$$1 \geq \alpha(I) = [0.24/\pi N(I)\eta][Q(0)/L(I)]$$

for the human TB tree; parabolic flow would be predicted in generation I airways when $\alpha(I) \leq 1$. Because of anatomical conditions, caution must be exercised in using $\alpha(I)$ and $\mathrm{Re}(I)$ values to designate locations of laminar-to-turbulent transition or a parabolic profile when fully developed flow is predicted, as discussed in the following text.

West and Hugh-Jones (*15*) have studied bronchial airflow patterns at 5 to 80 L/min tracheal flow rates (*sans* a larynx) in replica casts of the upper human TB tree. Turbulent airflow in the trachea began at a flow rate of 20 L/min; turbulence was attributed to airway branching and surface irregularities. Such airstream instabilities can probably be attributed to tracheal and large airway wall cartilagenous ring impressions. The turbulent motion was dampened on progression to distal airways. Laminar flow in lobar and distal bronchi and turbulent flow in proximal (to lobar) airways was observed for flow rates up to 40 L/min. When the flow rate was increased to 80 L/min, turbulence penetrated to segmental bronchi. The observation of laminar flow in distal (to segmental bronchi) airways at 80 L/min is consistent with theoretical predictions that may be extrapolated from the data in Table 1.

Dekker (*16*) studied the transition between laminar and turbulent flow in replica casts of the human trachea

Table 1. Airway dimensions and fluid dynamics parameters for the modified-Weibel morphology (8).

TB airway generation (I)	Length $L(I)$, cm	Diameter $D(I)$, cm	Mean inspiratory flow rate					
			$Q(0)$ = 15 L/min		$Q(0)$ = 30 L/min		$Q(0)$ = 60 L/min	
			$\alpha(I)$	Re(I)	$\alpha(I)$	Re(I)	$\alpha(I)$	Re(I)
0	10.494	1.574	1.24×10^{1}	1.38×10^{3}	2.48×10^{1}	2.75×10^{3}	4.95×10^{1}	5.50×10^{3}
1	4.163	1.067	1.56×10^{1}	1.01×10^{3}	3.12×10^{1}	2.03×10^{3}	6.24×10^{1}	4.06×10^{3}
2	1.662	0.726	1.95×10^{1}	7.46×10^{2}	3.91×10^{1}	1.49×10^{3}	7.82×10^{1}	2.98×10^{3}
3	0.665	0.490	2.44×10^{1}	5.52×10^{2}	4.88×10^{1}	1.10×10^{3}	9.77×10^{1}	2.21×10^{3}
4	1.111	0.394	7.31	3.43×10^{2}	1.46×10^{1}	6.87×10^{2}	2.92×10^{1}	1.37×10^{3}
5	0.936	0.306	4.34	2.21×10^{2}	8.68	4.42×10^{2}	1.74×10^{1}	8.85×10^{2}
6	0.787	0.245	2.58	1.38×10^{2}	5.16	2.76×10^{2}	1.03×10^{1}	5.52×10^{2}
7	0.665	0.201	1.53	8.42×10^{1}	3.05	1.68×10^{2}	6.11	3.37×10^{2}
8	0.560	0.163	9.06×10^{-1}	5.19×10^{1}	1.81	1.04×10^{2}	3.63	2.08×10^{2}
9	0.472	0.135	5.38×10^{-1}	3.13×10^{1}	1.08	6.27×10^{1}	2.15	1.25×10^{2}
10	0.402	0.114	3.16×10^{-1}	1.85×10^{1}	6.31×10^{-1}	3.71×10^{1}	1.26	7.42×10^{1}
11	0.341	0.095	1.86×10^{-1}	1.11×10^{1}	3.72×10^{-1}	2.23×10^{1}	7.44×10^{-1}	4.45×10^{1}
12	0.289	0.083	1.10×10^{-1}	6.37	2.20×10^{-1}	1.27×10^{1}	4.39×10^{-1}	2.55×10^{1}
13	0.236	0.072	6.72×10^{-2}	3.67	1.34×10^{-1}	7.34	2.69×10^{-1}	1.47×10^{1}
14	0.201	0.065	3.95×10^{-2}	2.03	7.89×10^{-2}	4.07	1.58×10^{-1}	8.13
15	0.175	0.058	2.27×10^{-2}	1.14	4.53×10^{-2}	2.28	9.06×10^{-2}	4.56
16	0.144	0.052	1.38×10^{-2}	6.35×10^{-1}	2.75×10^{-2}	1.27	5.51×10^{-2}	2.54

and main bronchi with and without a larynx. Flow was laminar for steady flow rates up to 21 L/min without a larynx. The inclusion of a larynx, however, caused turbulence at 6 L/min. Flow instabilities at the narrow glottis opening may have been of sufficient intensity to cause full-scale turbulence at such a low flow rate.

Schroter and Sudlow (*17*) measured airflow patterns in bifurcations within idealized models of human bronchi. A bifurcation, or airway branching site, is a region of complex geometry that consists of a tapering transition zone between airways of different diameter and a flow divider (carina). At all physiologically realistic flow rates, laminar but asymmetric flow patterns were observed; double vortex secondary currents may be the cause of such skewed profiles. The authors suggest, therefore, that it is not acceptable to assume a laminar parabolic flow profile in the "nominal laminar" region of the TB tree, which lies between the trachea and first few generations of large bronchi, to airways where $1 < \mathrm{Re} < 10$ (see Table 1).

An airflow pattern that is used to study aerosol deposition in the human TB tree must attempt to account for cartilagenous rings, bifurcations, and, perhaps most importantly, flow instabilities induced at the larynx. Taking the above investigations into account, we assume laminar plug flow for generations 0–4 (trachea and main, lobar, segmental, and first subsegmental bronchi) at flow rates <6 L/min and for generations 5–16 at all flow rates. Turbulent airflow is assumed in generations 0–4 at flow rates >6 L/min.

Particle Deposition

The following terminology is used in describing theoretical and empirical particle deposition efficiency equations:

ρ = particle density, g/cm^3
D_g = particle geometric diameter, μm
Q = mean inspiratory flow rate, L/min
λ = mean free path of air = 7.0×10^{-6} cm
G = gravitational constant = 980 cm/sec^2
T = absolute temperature, 293°K
k = Boltzmann constant = 1.38×10^{-16} g-cm^2/sec^{-2}-molecule-°K
$L(I)$ = length of generation I airway, cm
$R(I)$ = radius of generation I airway, cm
η = air kinematic viscosity = 1.5×10^{-1} cm^2/sec
μ = air absolute viscosity = 1.84×10^{-4} g/cm-sec
$U(I)$ = mean air velocity in generation I airway, cm/sec
$\phi(I)$ = inclination of generation I airway with respect to the horizontal, °
$\theta(I)$ = angle of bend of generation I, °
Re(I) = airflow Reynolds number in generation I airway
= $2R(I)U(I)/\eta$, dimensionless
m = particle mass, g
$C(D_g)$ = particle slip correction factor
= $1 + A(2\lambda/D_g)$, dimensionless
where A = $1.257 + 0.4 \exp\{-1.1D_g/(2\lambda)\}$
τ = particle relaxation time
= $mC(D_g)/(3\pi\mu D_g)$, sec
V = particle Stokes terminal settling speed
= $G\tau$, cm/sec
d = particle diffusion coefficient
= $kT\tau/m$, cm^2/sec

Parameters are defined in their most commonly used units; in computations, however, they all obviously must be converted to a consistent dimensional system.

Inhaled particles must penetrate the upper respiratory tract (the oropharyngeal and nasopharyngeal compartments for mouth and nose breathing, respectively, and the larynx) before they deposit in distal lung regions. Empirical formulae that describe aerosol deposition in these regions have been discussed (*18*).

Oropharyngeal and nasopharyngeal deposition probability equations were based on data from exposure of

human test subjects (*19,20*). The probability of deposition after mouth breathing, $p(m)$, may be expressed as follows:

$$p(m) = \begin{cases} 0, & \rho D_g^2 Q < 1.67 \times 10^3 \\ -0.496 + 0.154 \log (\rho D_g^2 Q), & 1.67 \times 10^3 \leq \rho D_g^2 Q \leq 10^4 \\ -2.988 + 0.777 \log (\rho D_g^2 Q), & 10^4 < \rho D_g^2 Q < 8.3 < 10^4 \end{cases}$$

For nose breathing, particle losses can be expressed by the following equations:

$$p(n) = \begin{cases} 0, & \rho D_g^2 Q < 2.82 \times 10^2 \\ -1.15 + 0.47 \log (\rho D_g^2 Q), & 2.82 \times 10^2 \leq \rho D_g^2 Q < 10^4 \end{cases}$$

Aerosol losses in replica laryngeal casts have been measured (*21,22*). Data were fit by the following equation:

$$p(\mathrm{l}) = 0.0350 + 3.9\, Stk, \qquad 10^{-3} \leq Stk \leq 10^{-1}$$

with a correlation coefficient of 0.96; $p(\mathrm{l})$ is the deposition probability normalized to particles entering a cast. The particle Stokes number, Stk, in the larynx is defined as $Stk = \rho D_g^2 W/18\mu R$, where W is mean airstream velocity. R characterizes the laryngeal cast aperature. Chan et al. (*23*) reported an R value of 1.65 cm; these authors also proposed slightly different coefficients for the above equation.

By combining the above formulae, the filtering efficiency of the upper respiratory tract proximal to TB airways can be described. For example, if the actual inhaled aerosol mass is expressed by M, the quantity that penetrates the larynx for nasal breathing, M_n, may be written as follows:

$$M_n = M[1 - p(n)][1 - p(l)]$$

The larynx significantly influences inhaled particle behavior in the following ways: turbulence created at the glottis opening can affect particle trajectories in the trachea and distal airways; also, particles entrained in a laryngeal jet may impact immediately downstream of the larynx, producing a deposition "hot spot."The following empirical equation describes this enhanced deposition:

$$p(t) = 2.536\, Stk^{1.231}$$

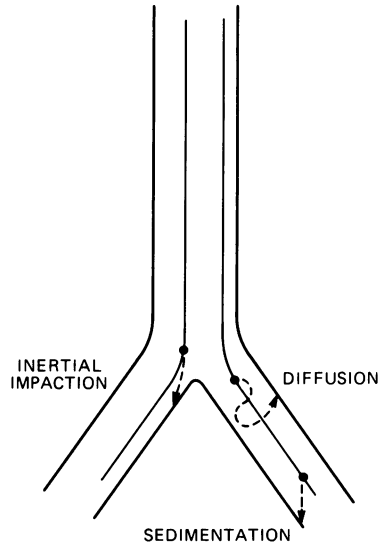

FIGURE 2. Action of the dominant deposition mechanisms in the lung: (——) primary air motion; (---) particle trajectories.

In this equation, $Stk = \rho D_g^2 W/9\mu D$, where D is the tracheal diameter.

In bronchial airways, inhaled particles are primarily deposited by the following mechanisms (see Fig. 2):

- Inertial impaction. When a particle possesses sufficient inertia, its trajectory will deviate from the entraining fluid at an airway branching site, resulting in impaction on the airway surface.
- Sedimentation. Particles of sufficient mass can be deposited under the action of gravity.
- Diffusion. Particles can also collide with airway surfaces subsequent to random Brownian motion; this mechanism is most efficient for submicrometer-sized particles.

Martonen (*5*) derived equations to calculate aerosol particle deposition probabilities in conducting airways of the human TB tree; their detailed explanation is beyond the scope of this paper. However, since the deposition efficiencies of the inertial impaction, sedimentation, and diffusion mechanisms (functions of particle size, density, and airflow patterns and rates) are central to this work, they are briefly outlined here.

Inertial Impaction. The following equation defines the probability of particle deposition at an airway bifurcation in a laminar air stream:

$$P(I) = \frac{2}{\pi}[e(1 - e^2)^{1/2} + \arcsin(e)]$$

where $e = \theta(I)\tau U(I)/2R(I)$. When airflow is turbulent, as observed in the trachea and upper bronchi,

$$P(I) = 1 - \exp\left\{\frac{-4e}{\pi}\right\}$$

In the trachea, $P(I)$ is assumed to be due to the action of the laryngeal jet.

Diffusion. For laminar airflow, particle deposition due to diffusion is expressed as

$$P(D) = 4\,(K/\pi)^{1/2} - K$$

where $K = dL(I)/U(I)R(I)^2$. The probability of particle deposition during turbulent air movement is

$$P(D) = 1 - \exp\left\{\frac{-0.022d^{3/4}\mathrm{Re}(I)^{7/8}L(I)}{U(I)R(I)^2}\right\}$$

Sedimentation. Conducting airways have different angles of orientation with respect to gravity. Residence time in an airway is defined by

$$t(I) = \frac{L(I)}{U(I) + V \sin\phi\,(I)}$$

when the airflow direction has a component aligned with the direction of action of gravity on a particle. If gravity and the vertical component of the air velocity are opposed, the time is

$$t(I) = \frac{L(I)}{U(I) - V \sin\phi\,(I)}$$

For laminar airflow, particle deposition probability is expressed by

$$P(S) = \frac{2}{\pi}\,[e(1 - e^2)^{1/2} + \arcsin(e)]$$

where $e = t(I)V\cos\phi(I)/2R(I)$. For unstable air flow,

$$P(S) = 1 - \exp\left\{\frac{-2\pi Gt(I)\cos\phi\,(I)}{\pi R(I)}\right\}$$

The division of aerosol mass at bifurcations is assumed to be proportional to airflow division and must be known before particle deposition efficiencies can be computed. In the Horsfield et al. (*7*) morphology, division is complicated because of the asymmetric branching pattern. In symmetric Weibel-type geometries, flow division at bifurcations is relatively simple to formulate. Details of the aerosol flow distribution patterns are defined in the Horsfield et al. (*7*) report.

In a previous study, Martonen (*24*) used the above deposition probability equations to evaluate the suitability of symmetric (*6,8*) and asymmetric (*7*) TB tree morphologies as representatives of adult human lungs. Theoretical aerosol deposition efficiencies and experimental data from nonhygroscopic aerosol inhalation exposure studies of Lippmann et al. (*9*) were compared.

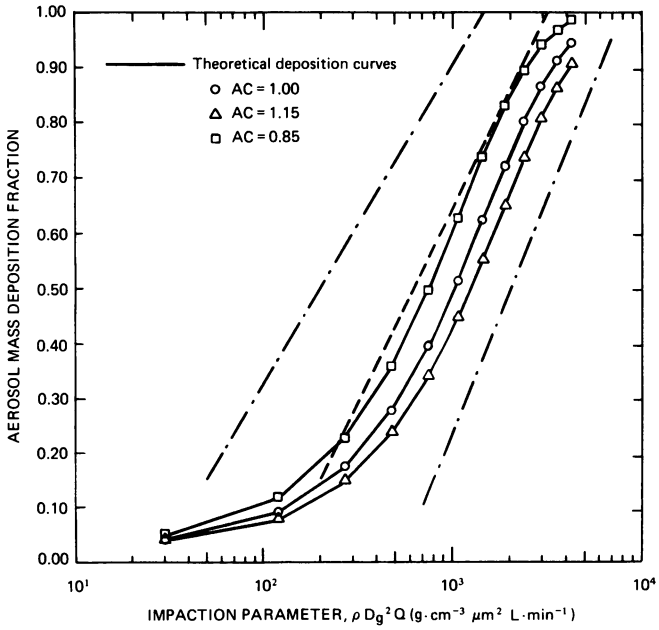

FIGURE 3. Nonhygroscopic aerosol inhalation exposure data compared to model calculations assuming a Weibel (*6*) TB tree morphology: (---) median fit of Lippmann et al. (*9*) to their experimental data; (–·–) limit lines to the data. From Martonen (*24*).

In Figures 3, 4, and 5, TB tree losses are graphed as a function of an impaction parameter, $\rho D_g^2 Q$. For each TB tree morphology, three airway coefficients (AC) were used to examine the effect of airway caliber on deposition. The AC = 1.00 curves correspond to published airway dimensions; AC = 0.85 curves correspond to airway diameters multiplied by 0.85; AC = 1.15 curves correspond to airway diameters increased 15%.

Theoretical calculations of aerosol deposition using symmetric TB tree morphologies agree well (Figs. 3 and 4) with experimental data that quantitate total dose delivered to the TB tree. Theoretical calculations using the asymmetric Horsfield et al. (*7*) TB tree geometry do not correlate well with experimental data (Fig. 5) since TB tree deposition is underestimated. The Soong et al. (*8*) morphology (Fig. 4) appears to be a particularly suitable description of the TB tree for use in aerosol deposition studies; the AC = 1.00 curve for $\rho D_g^2 Q > 300$ closely simulates the median fit to the experimental data. In addition, the abrupt curvature of the theoretical total TB tree deposition graphs at $\rho D_g^2 Q \simeq 300$ correlates with the experimental observations of Foord et al. (*25*). The systematic effect of a change in airway dimension, i.e., the translational shift of the total TB dose curves, suggests that intersubject differences may significantly influence inhalation exposure data.

Lippmann et al. (*9*) reported that the family of TB tree deposition curves for individuals was "s-shaped" when normalized to the quantity of aerosol mass entering the trachea; the curves appeared to be approaching asymptotes of ≈20 and ≈90% deposition. The midregions of the curves were quite linear with the slopes

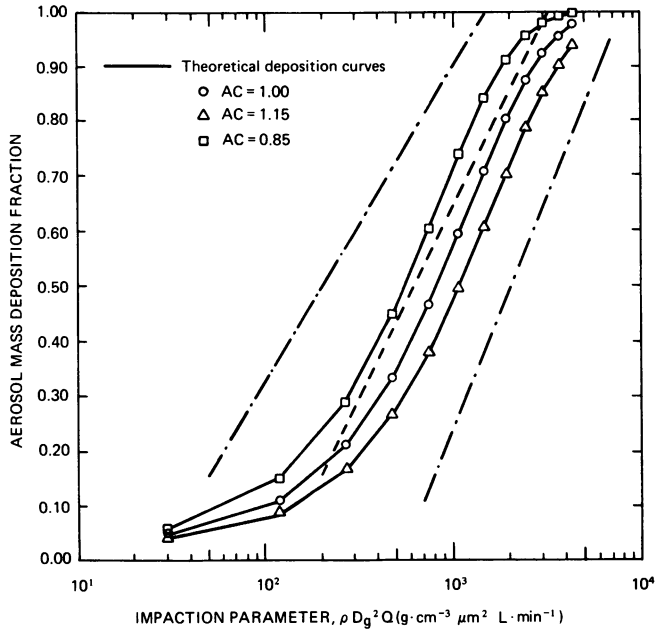

FIGURE 4. Nonhygroscopic aerosol inhalation exposure data compared to model calculations assuming a Soong et al. (*8*) TB tree morphology: (---) median fit of Lippmann et al. (*9*) to their experimental data; (–·–) limit lines to the data. From Martonen (*24*).

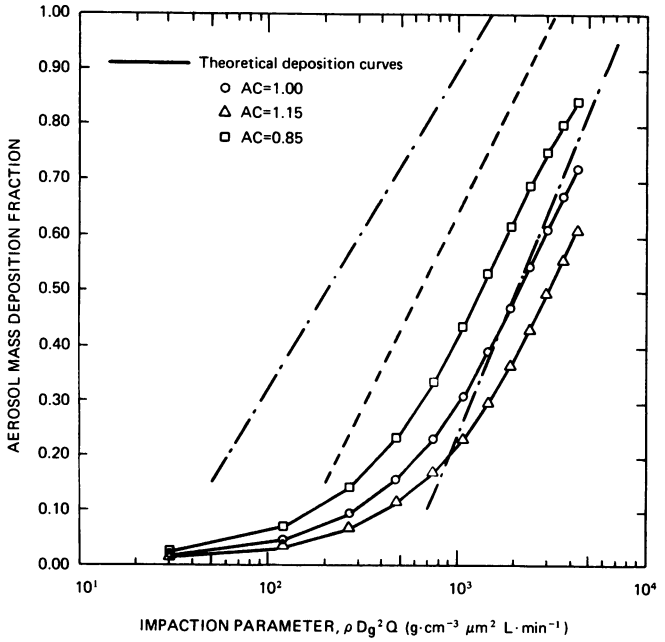

FIGURE 5. Nonhygroscopic aerosol inhalation exposure data compared to model calculations assuming a Horsfield et al. (*7*) TB tree morphology: (---) median fit of Lippmann et al. (*9*) to their experimental data; (–·–) limit lines to the data. From Martonen (*24*).

varying little among individuals. The families of theoretical curves in Figures 3 and 4 have the sigmoidal shape of the experimental curves, although asymptotes appear to be at ≈5 and ≈95% deposition, and the curves are practically parallel in their midregions. The theoretical curves in Figure 5 do not compare as well with data from experiments: they appear to be approaching a lower asymptote of ≈0%, only the AC = 0.85 curve appears to have an upper asymptote, and the curves are not linear or parallel in their midregions.

Temperature and Relative Humidity Profiles

A systematic (airway-by-airway) mapping of T and RH profiles in human test subjects has not been reported in the open literature, and available data on T and RH conditions in man vary greatly, as discussed in the following text. Ingelstedt (*26*) reviewed the published literature, explained anomalies and discussed differences between reported findings, and concluded that in future investigations: T and RH data must be collected *in situ* (i.e., not inferred from external observations); T and RH values must be simultaneously measured; and anesthesia should be avoided if possible.

To date, few investigations have satisfied these stringent criteria. After instruments were surgically implanted, Ingelstedt (*26*) simultaneously measured T and RH values in the laryngeal cavity (a fixed location) within numerous unanesthetized humans. For nasal breathing at room conditions (23°C, 30% RH), mean temperatures of 32°C (inspiration) and 36°C (expiration) were recorded; mean RH values were 98–99% during both phases of the respiratory cycle. For oral breathing, mean temperatures were 31°C (inspiration) and 36°C (expiration); however, mean RH values were very different during inspiration and expiration, 90% and 99%, respectively. Ferrus et al. (*27*) measured respiratory water loss and similarly concluded that the overall expired tidal volume is not fully water saturated.

A variety of experimental and theoretical techniques have been used by investigators to estimate T and RH profiles in the human respiratory tract. Déry et al. (*28*) used invasive techniques to record T and RH data at locations in bronchial airways. These authors measured profiles in the trachea and large airways of anesthetized humans with a flexible microthermistor probe. Breathing was through an endotracheal tube, thereby bypassing the nose. Mean tracheal T and RH values were 31°C and 86% (i.e., 4% less than Ingelstedt's (*26*) value), respectively, during inspiration. Mean T and RH values were 33°C and 91%, respectively, at a distance 10 cm distal to the main carina. Assuming the influence of anesthesia is general [the use of anesthesia may cause changes in the production and secretion of mucus (*29*)], an RH of approximately 95% may be proposed for unanesthetized humans at this location, in accordance with Ingelstedt's (*26*) work. In the Soong et al. (*8*) morphology, the 10-cm distance would include generation 7 airways. Ferron (*30*) assumed constant human bronchial

airway T and RH values of 37°C and 99.5%, respectively, for purposes of aerosol modeling; the RH value can be determined either from osmotic pressure or the lowering of the freezing point of blood. From theoretical considerations, Wilson and LaMer (*31*) and Milburn et al. (*32*) estimated ambient T and RH conditions inside the human lung to be about 37°C and 96%, respectively. Proctor (*33*) concluded that inhaled air is sufficiently warmed and humidified so that it reaches final body T and 99% RH at the alveolar level; alveolated airways begin at generation 17 in the Soong et al. (*8*) morphology. Using replica respiratory tract casts, Olson et al. (*34*) demonstrated that the T of inhaled air at the entrance to the trachea was within 0.2°C of the equilibrium T, 37°C, within the deep lung. Recent theoretical and experimental studies (*35,36*) support the concept of a gradation in RH profiles (to saturation) in the upper conducting airways of man for normal breathing in a moderate environment.

The possibility of transient supersaturation in upper bronchi under general ambient T and RH conditions has been postulated, based on theoretical descriptions of heat and water vapor transport in laminar (*37*) and disturbed laminar (*38*) flow fields. The models, however, neglect known laryngeal jet-related turbulent flow in upper human airways. The findings of Ingelstedt and Toremalm (*39,40*), who experimentally studied airflow patterns and heat transfer in airway models, indicate that larynx effects cannot be omitted from mathematical descriptions of inhaled gases, particularly because of boundary layer development considerations. The boundary layer thickness is of great biological importance because of the interchange of heat and moisture between air and mucous membranes. Ingelstedt and Toremalm (*39*) surmised a buffer layer interface between a laminar boundary layer and turbulent core flow to be a physiologically realistic simulation of upper airway fluid dynamics.

Ingelstedt (*26*) cited limited data suggesting that supersaturation might occur under highly unusual thermodynamic conditions (breathing in a cold chamber) because of insufficient condensation nuclei in the inspired laboratory air (0–4°C, 50–60% RH). However, he postulated from scientific principles that "...oversaturation can never occur in experiments at room temperature," and indeed, supersaturation could not be detected in his tests. A later study again experimentally confirmed the absence of supersaturation during the breathing of room air (*39*). Ferron's (*38*) theoretical model may become compatible with experimental data if it were refined to include the coupling of D_C (the diffusion coefficient of water vapor molecules in air) and D_T (the thermal diffusivity of air), and specific treatment of the thermodynamics of gas-particle interactions in the creation of T and RH profiles in human airways. However, influences of mixing effects attributable to the laryngeal jet and related flow disturbances *in vivo*, absent in the theory, argue against the plausibility of the phenomenon of supersaturation occurring during the inhalation of ambient aerosols.

Using the above experimental data as guidelines, two T and RH patterns were assumed in the current study in order to encompass most likely conditions that influence hygroscopic growth within the lung during inhalation of aerosols in a temperate (25°C and 50% RH) (*41*) environment. To simulate oral breathing, the RH of the trachea was assumed to be 90% and to monotonically increase 1% with each airway generation up to 99% at generation 9. The value of 99.5% was maintained for all distal airways. The constant value for peripheral airways is consistent with a state of equilibrium at those levels and is in agreement with the RH levels predicted from theoretical bases, as previously discussed. To simulate nasal breathing, we assumed that RH equilibrium conditions are attained in the trachea and remain at 99.5% in distal bronchial passages. For both modes of breathing, we assumed a constant temperature of 37°C in the TB tree, consistent with experimental data quantitating the extent of warming that occurs in the nasal and oral pharyngeal compartments.

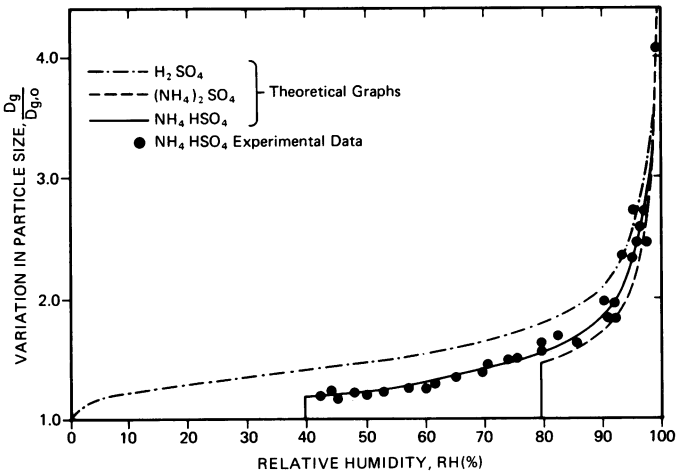

FIGURE 6. Hygroscopic growth curves of several submicrometer ambient sulfate aerosols of health effects concern. D_g and $D_{g,o}$ are the final droplet diameter at a given RH value and the original geometric particle diameter, respectively. Data from Tang and Munkelwitz (*11*).

Table 2. Influence of hygroscopic growth on deposition of ambient H_2SO_4 particles.

		Total deposition, %		
$D_{g,o}$, μm	Q, L/min	Nonhygroscopic	90–99.5% RH	99.5% RH
0.2	15	14.5	7.0	7.2
	30	10.6	5.3	5.9
	60	7.8	4.8	6.1
0.5	15	8.8	10.7	12.6
	30	6.8	9.5	13.3
	60	6.0	12.0	19.2
1.0	15	8.9	27.8	34.1
	30	8.0	26.5	38.2
	60	9.7	35.6	54.7

Ambient Aerosol Sizes and Growth Data

Chemical composition analyses of urban atmospheres sampled with cascade impactors have established that SO_4^{2-}, NO_3^-, and NH_4^+ ions are most often extracted from particulate matter with an ambient MMAD of 0.2 to 0.6 μm (*42*). During smog episodes, when a general increase in ambient levels of gaseous and total suspended particulate (TSP) pollutants is experienced, major differences in relative composition of the chemical constituents may occur. Israël et al. (*43*) report that "sulfate clouds" exist in which ~62% of the TSP is $(NH_4)_2SO_4$. Moreover, the particle mass distributions within such clouds had pronounced peaks in the 1- to 3-μm MMAD size range. Information present in the Inhalable Particulate Data Bank (*44*) clearly demonstrates that most particulate sulfate in urban aerosols is in the fine mode (<2.5 μm); maximum 24-hr ambient sulfate levels of about 40 to 45 $\mu g/m^3$ have been reported.

The hygroscopic growth of H_2SO_4, $(NH_4)_2SO_4$, and NH_4HSO_4 particles to final equilibrium sizes in precisely defined moist environments was investigated by Tang (*10*), Tang and Munkelwitz (*11*), and Tang et al. (*12*). Experimental data for NH_4HSO_4 aerosols and theoretical growth curves for all the aerosols are presented in Figure 6.

Calculations for 12 different salts (*30*) showed that particles of aerodynamic diameter, D_{ae}, ~0.2 μm may reach equilibrium diameters at 99.5% RH and 37°C conditions within 0.1 sec. Submicrometer ambient H_2SO_4, $(NH_4)_2SO_4$, and NH_4HSO_4 aerosols grow considerably during transit to the trachea by equilibrating to a high T and RH environment in the upper respiratory tract (*35,41*). For a tidal volume of 500 cm^3, the residence time of an inhaled particle in the nasopharyngeal region is approximately 0.09 sec. We will use the growth curves in Figure 6 to define particle parameters (size and density) as a function of assumed respiratory tract T and RH profiles.

Because best agreement between theoretical predictions of nonhygroscopic aerosol behavior and experimental deposition data is found with a Soong et al. (*8*) morphology, it will be used in our discussion of the effects of hygroscopic growth on inhaled pollutants. The size and density changes of an inhaled ambient particle during oral (90–99.5% RH) and nasal (99.5% RH) breathing simulations will be defined by the appropriate curve in Figure 6. Deposition in the TB tree, therefore, will be computed in a manner commensurate with stepwise changes in particle parameters along airways.

Effects of Hygroscopic Growth on Deposition

The complex influence of hygroscopic growth, as a function of assumed RH profile, on H_2SO_4 aerosol behavior is demonstrated in Table 2. Two observations can be made from the data: (a) particles in the diffusion-dominated regime have reduced deposition relative to nonhygroscopic particles of identical preinspired size, and (b) hygroscopic growth produces an increase in deposition, relative to nonhygroscopic particles, of particles primarily affected by inertial and gravitational forces. For the smallest particles, the disparity between nonhygroscopic and hygroscopic cases increases as the magnitude of Q decreases. This is consistent with the action of diffusion, the efficiency of which is related to the particle residence time in an airway. For the largest particles, however, the opposite occurs because particles grow sufficiently to become effectively deposited by inertial impaction; the efficiency of the mechanism is related to particle velocity. Differences between the two RH profiles are most pronounced at the largest particle size and flow rate tested. In the model, an ambient particle of initial particle size ($D_{g,0}$ = 1.0 μm grew to D_g = 2.1 μm within the trachea for oral breathing (90–99.5% RH) and finally attained D_g = 4.5 μm in generation 10. For nasal breathing (99.5% RH), the 4.5-μm size was assumed in the trachea and all distal bronchial passages.

The effect of an assumed RH profile on the distribution of deposited 0.5-μm particle H_2SO_4 aerosol mass as a function of Q is shown in Figure 7. The apparent common feature of panels *A*, *B*, and *C* of Figure 7 is that increasing the magnitude of Q increases the relative percentage of deposition in the larger conducting airways while yielding reduced losses in more peripheral airways. Interestingly, the crossover occurs within generations 11–14 for both RH profiles tested.

The variation in D_g of an originally sized 0.5-μm H_2SO_4 particle within the respiratory tract is presented in Figure 8 to explain deposition-related hygroscopic growth effects. For nasal breathing, growth to final equilibrium size is assumed to be complete following passage through the nasopharyngeal compartment. For mouth breathing, D_g is about 1 μm in the trachea and steadily increases until ≃ 2.2 μm is attained in generation 10 airways. Particles that are hygroscopic in character will absorb water vapor present in the humid environment of the respiratory tract. Subsequently, the particles will change in size and density while traversing airways; this is schematically illustrated in Figure 9. If only water vapor uptake is assumed to affect density (i.e., changes in crystalline physical state are ignored), then particle density may be expressed as

$$\rho = \rho_{H_2O} + (\rho_0 - \rho_{H_2O})(D_{g,0}/D_g)^3$$

where ρ_o and ρ_{H_2O} are the densities of the original particle and water, respectively.

At the lowest flow rate in Figure 7, total deposition does not vary much between *A*, *B*, and *C*. There is, however, a noticeable shift in mass fraction deposited in larger upstream airways with consideration of the influence of an assumed RH profile upon hygroscopic growth effects. At Q = 60 L/min, total deposition increases by a factor of 2 between *A* and *B* and increases by a factor of 3 between *A* and *C*. Moreoever, there is

Q (L·min^{-1})	Total Dose (%)	Relative Dispersion (%) 0 ⩽ I ⩽ 5	6 ⩽ I ⩽ 10	11 ⩽ I ⩽ 16
15	8.8	3.9	17.2	78.9
30	6.8	7.5	19.5	73.0
60	6.0	15.2	23.9	60.9

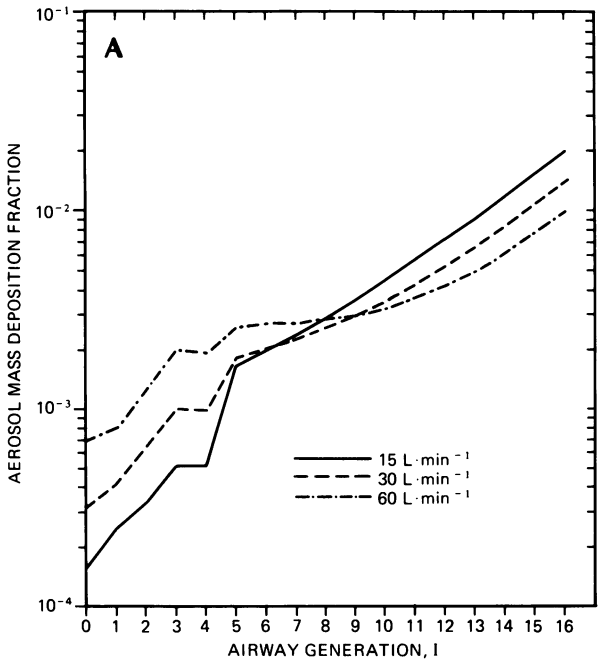

Q (L·min^{-1})	Total Dose (%)	Relative Dispersion (%) 0 ⩽ I ⩽ 5	6 ⩽ I ⩽ 10	11 ⩽ I ⩽ 16
15	10.7	6.4	18.8	74.8
30	9.5	13.0	28.4	58.6
60	12.0	19.9	37.5	42.6

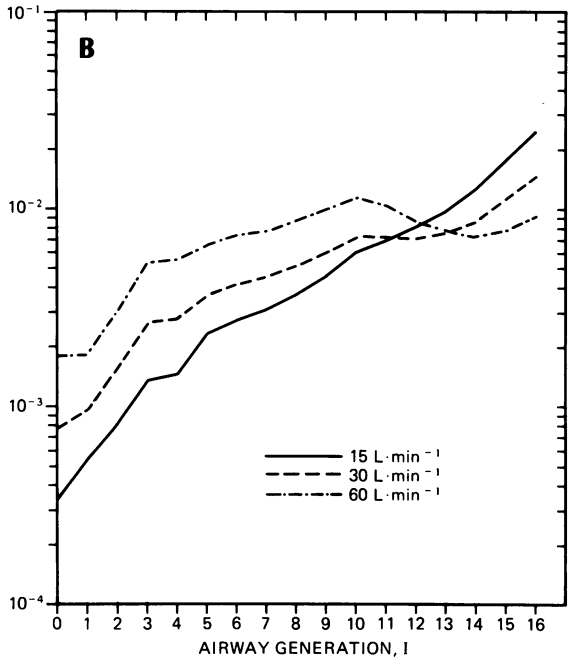

Q (L·min^{-1})	Total Dose (%)	Relative Dispersion (%) 0 ⩽ I ⩽ 5	6 ⩽ I ⩽ 10	11 ⩽ I ⩽ 16
15	12.6	16.4	21.7	61.9
30	13.3	29.6	30.1	40.3
60	19.2	40.1	35.4	24.5

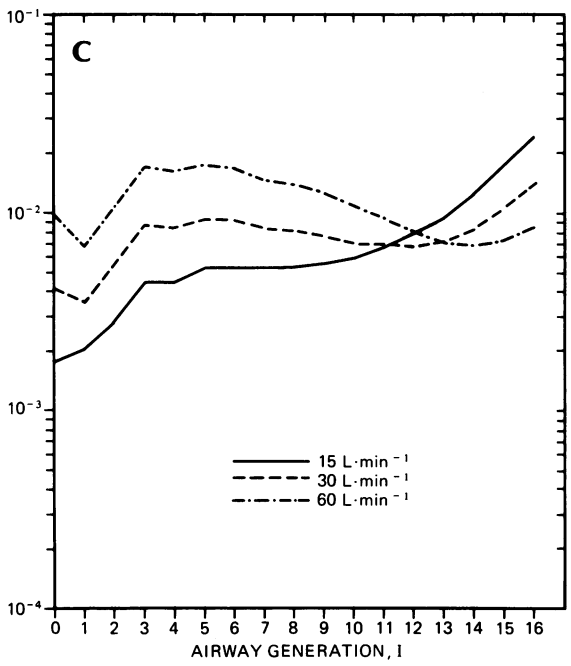

FIGURE 7. Influence of inspiratory flow rate on the relative percent dispersion of the total dose of ambient 0.5-μm $D_{g,0}H_2SO_4$ particles for different RH profiles in the TB tree: (*A*) nonhygroscopic particle behavior included for comparison; (*B*) 90–99.5% RH; (*C*) 99.5% RH.

a decided proximal shift in inter-TB distribution at the highest flow rate.

Whether or not hygroscopic growth increases total dose delivered to conducting airways depends on the original size of an inhaled aerosol. This is illustrated in Figure 10 for $(NH_4)_2SO_4$. The data suggest that a critical size, D_c, exists. If $D_{g,0} > D_c$, hygroscopic effects increase deposition (relative to nonhygroscopic particles

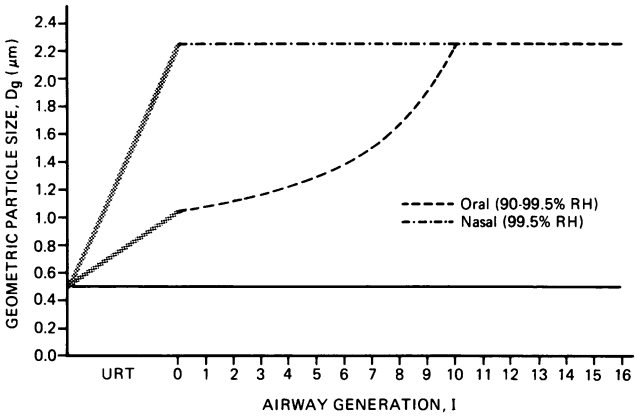

FIGURE 8. Change in diameter of a submicrometer ($D_{g,0}$ = 0.5 μm) H_2SO_4 particle for various breathing modes: (—) nonhygroscopic particle behavior included for comparison. URT denotes upper respiratory tract.

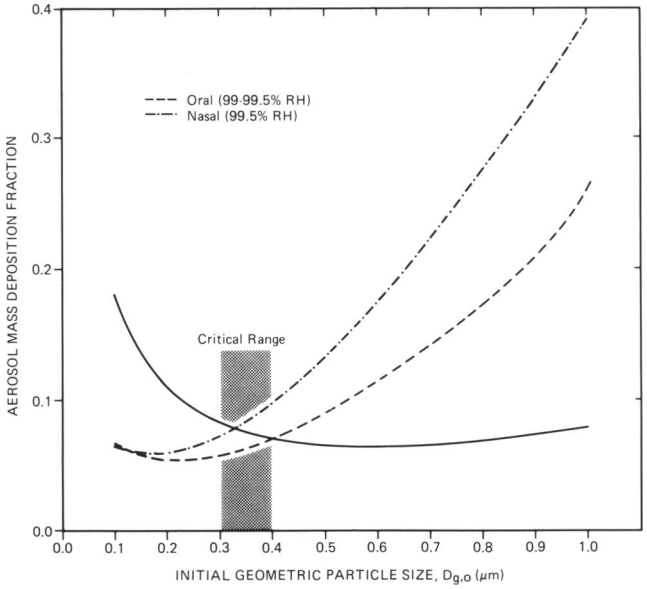

FIGURE 10. The influence of inhaled particle size and breathing mode on $(NH_4)_2SO_4$ aerosol deposition: (—) nonhygroscopic particle behavior included for comparison. Q = 30 L/min.

of like size); if smaller-sized particles are inhaled, the influence of growth is to reduce deposition.These observations may be explained by changes in the relative effectiveness of the major particle deposition efficiency mechanisms, which have been formulated in terms of particle parameters. In Figure 11, the effects of changing particle size and density following mouth breathing are illustrated. In Figure 11*A*, where $D_{g,0}$ = 0.2 μm, nonhygroscopic particles are deposited primarily by diffusion; hygroscopicity results in relatively reduced dosage due to the increase in particle size. In Figure 11*B*, where $D_{g,0}$ = 0.8 μm, nonhygroscopic particles are deposited by inertial impaction in upper airways and diffusion in lower airways. An increase in total deposition concomitant with growth results from increased deposition due to larger particle mass that more than compensates for a reduction in the efficiency of deposition due to Brownian motion.

Relative humidity effects on $(NH_4)_2SO_4$ aerosol distribution are illustrated in Figure 12. In Figure 12*A*, total deposition is almost the same for a nonhygroscopic aerosol and $(NH_4)_2SO_4$ assuming oral (90–99.5% RH) breathing. The percent of the total aerosol mass delivered to upper airways, however, is approximately double due to growth by water vapor absorption; this occurs at the expense of dose delivered to the lower airways. For nasal breathing (99.5% RH), $(NH_4)_2SO_4$ distribution to upper airways is more than double that for oral breathing; in this instance, distribution is now nearly uniform within the TB tree. The situation is different for the larger particles. Hygroscopic growth in the 90 to 99.5% RH profile produces a total deposition that increases by nearly a factor of 3 relative to nonhygroscopic aerosols, but relative dispersion among airways is not as affected. Growth in the 99.5% RH profile leads to an increase of more than a factor of 4 in total aerosol mass deposited; the percent of the total delivered to upper airways is more than double that for oral breathing.

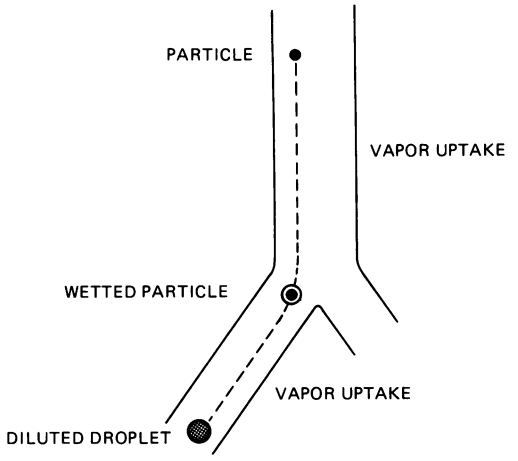

FIGURE 9. Hygroscopic particle growth in the humid bronchial atmosphere.

Figures 13 and 14 illustrate some of the complex effects of hygroscopic growth assumptions, $D_{g,0}$, and Q on the total dose and regional distribution of inhaled NH_4HSO_4 relative to the total mass intake at the trachea (I = 0). For example, the regional distribution of orally inspired pollutant for Q = 15 L/min (Fig. 13*B*) is skewed towards lower airways; doses here are factors of 10 to 30 greater than those of upper airways and factors of ~4 greater than those of middle airways. In addition, as $D_{g,0}$ increases from 0.1 to 1.0 μm, total dose increases from ~9 to ~27% of TB intake. Nasal breathing (Fig. 13*C*) is qualitatively similar to oral breathing, except that regional distribution is not as skewed for 1.0-μm particles. Comparison of nonhygroscopic results

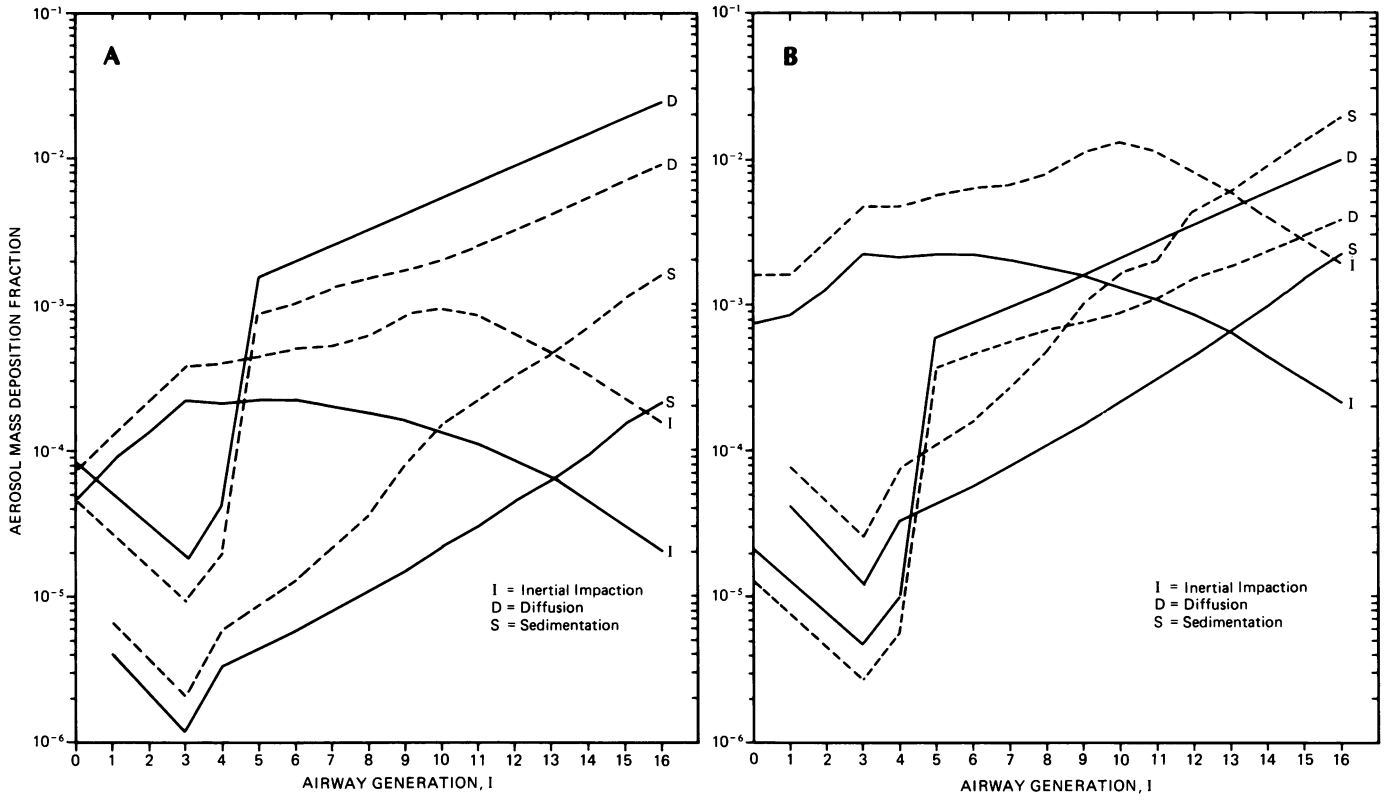

FIGURE 11. Relative efficiencies of the dominant aerosol deposition mechanisms as a function of ambient size: (---) oral breathing of $(NH_4)_2SO_4$ particles is simulated; (—) nonhygroscopic particle behavior included for comparison. (*A*) $D_{g,0}$ = 0.2 μm; (*B*) $D_{g,0}$ = 0.8 μm; Q = 30 L/min.

(Fig. 13*A*) with the two hygroscopic results (Figs. 13*B* and *C*) reveals differences: the nonhygroscopic assumption overestimates total dose by a factor of 2 to 3 for small particles (0.1 μm) and underestimates by a factor of ~1/3 for large particles (1.0 μm); furthermore, the nonhygroscopic assumption predicts an overall decrease in total dose with increasing particle size, while both hygroscopic assumptions predict an overall increase. Similarities exist between the nonhygroscopic, oral, and nasal cases: regional distribution for 0.1-, 0.5-, and 1.0-μm particles is consistently skewed to lower airways, and total dose for 0.5-μm particles is similar in each case.

Figure 14 illustrates total dose and regional distribution of NH_4HSO_4 for Q = 60 L/min. Comparison of Figures 13 and 14 reveals effects due in part to flow rate. For example, regional distribution of orally inspired NH_4HSO_4 (Fig. 14*B*) is less skewed in lower airways than in Figure 13*B*, especially as $D_{g,0}$ increases. Regional distribution for nasal breathing (Fig. 14*C*) becomes skewed towards upper airways as $D_{g,0}$ increases; for 1.0-μm particles, upper airway dose is a factor of ~ 1.5 greater than the middle airway dose and a factor of more than 3 greater than the lower airway dose. Under nonhygroscopic conditions (Fig. 14*A*), total dose for small particles is overestimated and total dose for large particles is underestimated; regional distribution for large particles is uniform.

Thus, variation of hygroscopic growth assumptions, $D_{g,0}$, or Q can produce complex effects on deposition. When hygroscopic growth (oral or nasal) is assumed, total dose is proportional to $D_{g,0}$. However, when no hygroscopic growth is assumed, total dose tends to at first decrease and then increase with increasing $D_{g,0}$. In addition, hygroscopic growth can lead to predominantly upper airway or lower airway deposition, depending on the breathing mode (nasal or oral).

Summary

Nonhygroscopic aerosol deposition computations using a theoretical model agree well with the Lippmann et al. (*9*) median fit to their experimental measurements, indicating that *in vivo* particle behavior is being accurately simulated (see Fig. 4). Airway diameters are varied in the model to examine the effect of intersubject variability within a population. For individual human subjects, experimentally determined total deposition curves have characteristic "s-shapes" that, within a population, have similar asymptotes and almost parallel, linear midsections. Significantly, the theoretical model generates the general sigmoidal shapes of such individual TB deposition patterns and accurately calculates the slopes of their quasi-linear segments and the positions

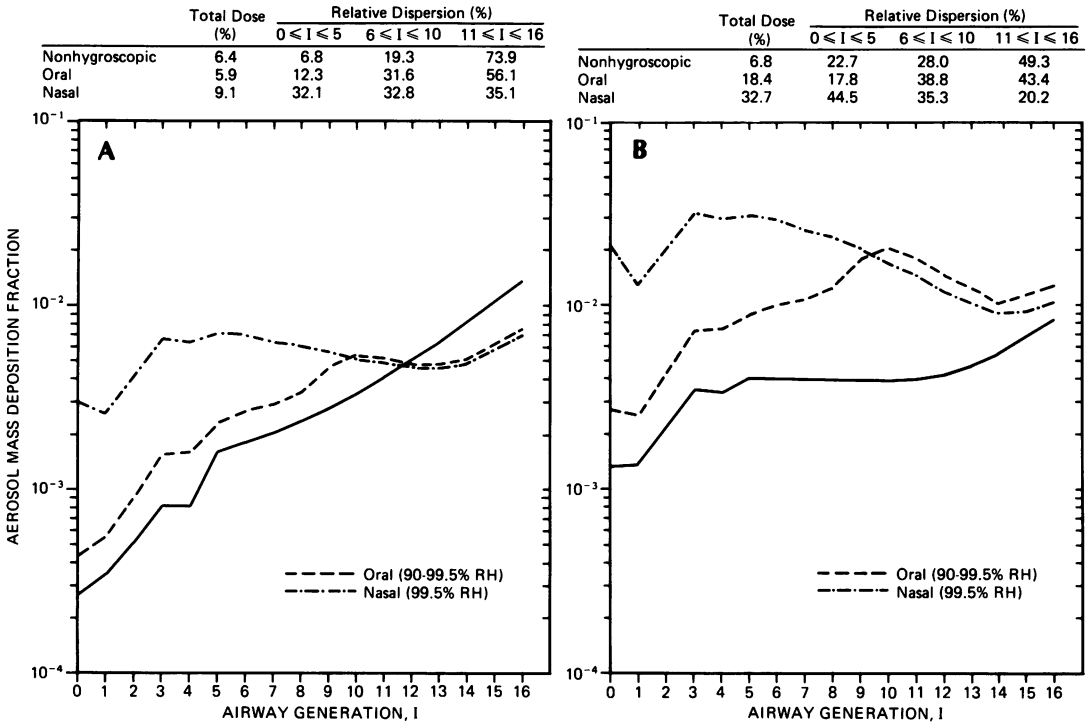

FIGURE 12. Influence of RH profiles on the relative percent dispersion of the total dose of $(NH_4)_2SO_4$ particles: (*A*) $D_{g,o}$ = 0.3 μm; (*B*) $D_{g,o}$ = 0.7 μm. Q = 60 L/min; (—) nonhygroscopic particle behavior included for comparison.

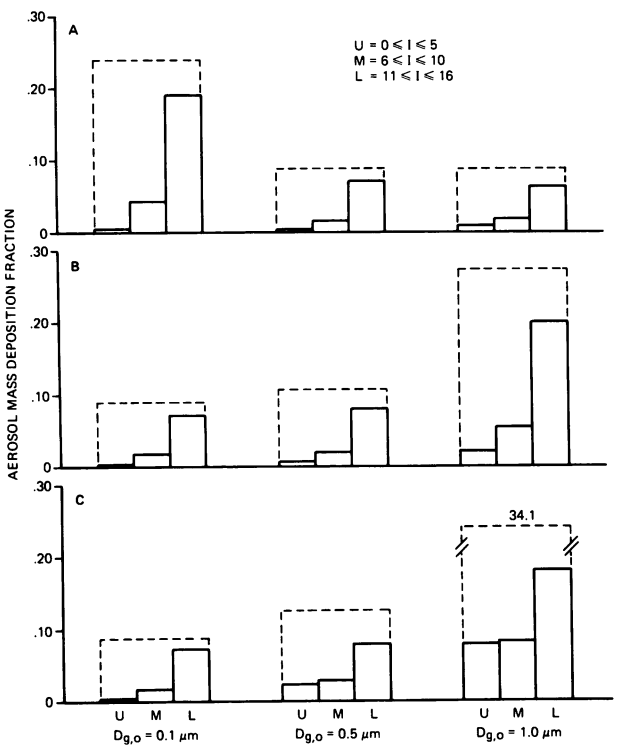

FIGURE 13. Influence of RH profile and $D_{g,o}$ on (---) total dose and (—) regional distribution of NH_4HSO_4 aerosols inhaled at Q = 15 L/min: U = upper, M = middle, and L = lower airways. *I* denotes airway generation. (*A*) nonhygroscopic particle behavior included for comparison; (*B*) 90–99.5% RH; (*C*) 99.5% RH.

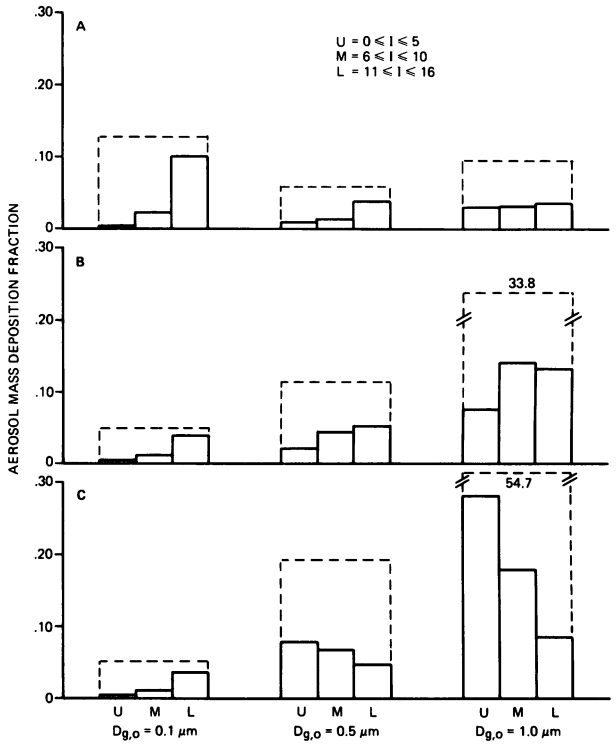

FIGURE 14. Influence of RH profile and $D_{g,o}$ on (---) total dose and (—) regional distribution of NH_4HSO_4 inhaled at Q = 60 L/min: U = upper, M = middle, and L = lower airways. *I* denotes airway generation. (*A*) nonhygroscopic particle behavior included for comparison; (*B*) 90–99.5% RH; (*C*) 99.5% RH.

of their two asymptotes.

The experimental and theoretical hygroscopic growth data of Tang and Munkelwitz (*11*) are incorporated into the aforementioned validated model to compute the influence of hygroscopicity on the deposition of ambient sulfate aerosols. The primary factors requiring definition prior to studying possible growth effects are initial particle geometry and density, material hygroscopic growth characteristics, respiratory parameters, and T and RH profiles. The influences of hygroscopic growth on inhaled aerosol behavior are very complex; both the total mass deposited and its regional dispersion may be significantly affected. The factor of hygroscopicity, therefore, is an important factor in the hazard evaluation of atmospheric particulate matter of health effects concern.

This report has been reviewed by the Health Effects Research Laboratory, U.S. Environmental Protection Agency, and approved for publication. Mention of trade names or commercial products does not constitute endorsement or recommendation for use. This work was sponsored by EPA Contract No. 68-02-2566.

REFERENCES

1. Husar, R. B., Lodge, J. P., Jr., Klug, W., and Moore, D. J. (Eds.). Sulfur in the Atmosphere. Proceedings of the International Symposium. Atmos. Environ. 12: 1–796 (1978).
2. NRC-NAS Committee on Sulfur Oxides. Sulfur Oxides. National Research Council, National Academy of Sciences, Washington, DC, 1978, pp. 130–179.
3. Task Group on Lung Dynamics. Deposition and retention models for internal dosimetry of the human respiratory tract. Health Phys. 2: 173–207 (1966).
4. Lippmann, M., and Albert, R. E. The effects of particle size on the regional distribution of inhaled aerosols in the human respiratory tract. Am. Ind. Hyg. Assoc. J. 30: 257–275 (1969).
5. Martonen, T. B. Analytical model of hygroscopic particle behavior in human airways. Bull. Math. Biol. 44: 425–442 (1982).
6. Weibel, E. R. Morphometry of the Human Lung. Springer-Verlag, Berlin, 1963.
7. Horsfield, K., Dart, G., Olson, D. E., Filley, G. F., and Cumming, G. Models of the human bronchial tree. J. Appl. Physiol. 31: 207–217 (1971).
8. Soong, T. T., Nicholaides, P., Yu, C. P., and Soong, S. C. A statistical description of the human tracheobronchial tree geometry. Respir. Physiol. 37: 161–172 (1979).
9. Lippmann, M., Albert, R. E., and Peterson, H. T. The regional deposition of inhaled aerosols in man. In: Inhaled Particles III (W. H. Walton, Ed.), Gresham Press, Unwin Bros., England, 1971, pp. 105–122.
10. Tang, I. N. Phase transformation and growth of aerosol particles composed of mixed salts. J. Aerosol Sci. 7: 361–371 (1976).
11. Tang, I. N., and Munkelwitz, H. R. Aerosol growth studies—III. Ammonium bisulfate aerosols in a moist atmosphere. J. Aerosol Sci. 8: 321–329 (1977).
12. Tang, I. N., Munkelwitz, H. R., and Davis, J. G. Aerosol growth studies. II. Preparation and growth measurements of monodisperse salt aerosols. J. Aerosol Sci. 8: 149–159 (1977).
13. Pedley, T. J., Schroter, R. C., and Sudlow, M. F. Gas flow and mixing in the airways. In: Bioengineering Aspects of the Lung (John B. West, Ed.), Marcel Dekker, New York, 1979, pp. 163–265.
14. Langhaar, H. L. Steady flow in the transition length of a straight tube. J. Appl. Mech. 9: 55–58 (1942).
15. West, J. B., and Hugh-Jones, P. Patterns of gas flow in the upper bronchial tree. J. Appl. Physiol. 14: 753–759 (1959).
16. Dekker, E. Transition between laminar and turbulent flow in human trachea. J. Appl. Physiol. 16: 1060–1064 (1961).
17. Schroter, R. C., and Sudlow, M. F. Flow patterns in models of the human bronchial airways. Respir. Physiol. 7: 341–355 (1969).
18. Martonen, T. Deposition of inhaled particulate matter in the upper respiratory tract, larynx, and bronchial airways: a mathematical description. J. Toxicol. Environ. Health 12: 787–800 (1983).
19. Lippmann, M. Regional deposition of particles in the human respiratory tract. In: Handbook of Physiology: Reaction to Environmental Agents (D. H. K. Lee, Ed.), Williams and Wilkins, Baltimore, 1977, pp. 213–232.
20. Heyder, J. Particle transport onto human airway surfaces. Eur. J. Respir. Dis. 63 (Suppl. 119): 29–50 (1982).
21. Martonen, T. B. Measurement of particle dose distribution in a model of a human larynx and tracheobronchial tree. J. Aerosol Sci. 14: 11–22 (1983).
22. Martonen, T. B., and Lowe, J. Assessment of aerosol deposition patterns in human respiratory tract casts. In: Aerosols in the Mining and Industrial Work Environments (V. A. Marple and B. Y. H. Liu, Eds.), Ann Arbor Science, Ann Arbor, MI, 1983, pp. 151–164.
23. Chan, T. L., Schreck, R. M., and Lippmann, M. Effect of the laryngeal jet on particle deposition in the human trachea and upper bronchial airways. J. Aerosol Sci. 11: 447–459 (1980).
24. Martonen, T. B. On the fate of inhaled particles in the human: a comparison of experimental data with theoretical computations based on a symmetric and asymmetric lung. Bull. Math. Biol. 45: 409–424 (1983).
25. Foord, N., Black, A., and Walsh, M. Regional deposition of 2.5–7.5 μm diameter inhaled particles in healthy male nonsmokers. J. Aerosol Sci. 9: 343–357 (1978).
26. Ingelstedt, S. Studies on the conditioning of air in the respiratory tract. Acta Oto-Laryng. (Suppl.) 131: 1–80 (1956).
27. Ferrus, L., Guenard, H., Vardon, G., and Varene, P. Respiratory water loss. Respir. Physiol. 39: 367–381 (1980).
28. Déry, R., Pelletier, J., Jacques, A., Clavet, M., and Houde, J. J. Humidity in anaesthesiology. III. Heat and moisture patterns in the respiratory tract during anaesthesia with the semi-closed system. Can. Anaes. Soc. J. 14: 287–298 (1967).
29. Han, Y. H., and Lowe, H. J. Humidification of inspired air. J. Am. Med. Assoc. 205: 91–95 (1968).
30. Ferron, G. A. The size of soluble aerosol particles as a function of the humidity of the air. Application to the human respiratory tract. J. Aerosol Sci. 8: 251–267 (1977).
31. Wilson, I. B., and LaMer, V. K. Retention of aerosol particles in the human respiratory tract as a function of particle radius. J. Ind. Hyg. Toxicol. 30: 265–280 (1948).
32. Milburn, R. H., Crider, W. L., and Morton, S. D. The retention of hygroscopic dusts in the human lungs. Am. Med. Assoc. Arch. Ind. Health 15: 59–62 (1957).
33. Proctor, D. F. Physiology of the upper airways. In: Handbook of Physiology, Sec. 3, Respiration. American Physiological Society, Washington, DC, 1964.
34. Olson, D. E., Sudlow, M. F., Horsfield, K., and Filley, G. F. Convective patterns of flow during inspiration. Arch. Intern. Med. 131: 51–57 (1973).
35. Hanna, L. M., and Scherer, P. W. Analysis of respiratory heat and water transport. Proceedings 35th Annual Conference on

Engineering in Medicine and Biology. 24: 132 (1982).
36. Nuckols, M. L. Heating and humidification of gases within the human airways. Proceedings 35th Annual Conference on Engineering in Medicine and Biology. 24: 133 (1982).
37. Höllander, W. Transient supersaturation in the human airways and its effect on inhaled particle growth and deposition. In: Abstracts of the American Industrial Hygiene Conference, Chicago, 1979, p. 90.
38. Ferron, G. A. Calculation of the relative humidity in the upper human airways, in relation to the aerosol particle growth. International Symposium on Deposition and Clearance of Aerosols in the Human Respiratory Tract, Bad Gleichenberg, Austria, 1981, Part 1: 14–17.
39. Ingelstedt, S., and Toremalm, N. G. Aerodynamics within the larynx and trachea. Indications for vapour therapy in acute laryngo-tracheitis. Acta Oto-Laryng. (Suppl.) 158: 81–92 (1960).
40. Ingelstedt, S., and Toremalm, N. G. Air flow patterns and heat transfer within the respiratory tract. Acta Physiol. Scand. 51: 204–217 (1961).
41. Walker, J. E. C., Wells, R. E., Jr., and Merrill, E. W. Heat and water exchange in the respiratory tract. Am. J. Med. 30: 259–267 (1961).
42. Patterson, R. K., and Wagman, J. Mass and composition of an urban aerosol as a function of particle size for several visibility levels. J. Aerosol Sci. 8: 269–279 (1977).
43. Israël, G. W., Bauer, H.-W., and Wengenroth, K. Physical and chemical characteristics of suspended particulates during smog episodes. J. Aerosol Sci. 14: 260–264 (1983).
44. U. S. Environmental Protection Agency. Inhalable Particulate Data Bank. Environmental Monitoring Systems Laboratory, U. S. Environmental Protection Agency, Research Triangle Park, NC, 1984.